The Astrophysical Journal, 678:1165–1179, 2008 May 10

THE ALL-PARTICLE SPECTRUM OF PRIMARY COSMIC RAYS IN THE WIDE ENERGY RANGE FROM 10^{14} TO 10^{17} eV OBSERVED WITH THE TIBET-III AIR-SHOWER ARRAY

M. Amenomori,[1] X. J. Bi,[2] D. Chen,[3] S. W. Cui,[4] Danzengluobu,[5] L. K. Ding,[2] X. H. Ding,[5] C. Fan,[6] C. F. Feng,[6] Zhaoyang Feng,[2] Z. Y. Feng,[7] X. Y. Gao,[8] Q. X. Geng,[8] H. W. Guo,[5] H. H. He,[2] M. He,[6] K. Hibino,[9] N. Hotta,[10] Haibing Hu,[5] H. B. Hu,[2] J. Huang,[11] Q. Huang,[7] H. Y. Jia,[7] F. Kajino,[12] K. Kasahara,[13] Y. Katayose,[3] C. Kato,[14] K. Kawata,[11] Labaciren,[5] G. M. Le,[15] A. F. Li,[6] J. Y. Li,[6] Y.-Q. Lou,[16] H. Lu,[2] S. L. Lu,[2] X. R. Meng,[5] K. Mizutani,[13,17] J. Mu,[8] K. Munakata,[14] A. Nagai,[18] H. Nanjo,[1] M. Nishizawa,[19] M. Ohnishi,[11] I. Ohta,[20] H. Onuma,[17] T. Ouchi,[9] S. Ozawa,[11] J. R. Ren,[2] T. Saito,[21] T. Y. Saito,[22] M. Sakata,[12] T. K. Sako,[11] M. Shibata,[3] A. Shiomi,[9,11] T. Shirai,[9] H. Sugimoto,[23] M. Takita,[11] Y. H. Tan,[2] N. Tateyama,[9] S. Torii,[13] H. Tsuchiya,[24] S. Udo,[11] B. Wang,[8] H. Wang,[2] X. Wang,[11] Y. Wang,[2] Y. G. Wang,[6] H. R. Wu,[2] L. Xue,[6] Y. Yamamoto,[12] C. T. Yan,[11] X. C. Yang,[8] S. Yasue,[25] Z. H. Ye,[15] G. C. Yu,[7] A. F. Yuan,[5] T. Yuda,[9] H. M. Zhang,[2] J. L. Zhang,[2] N. J. Zhang,[6] X. Y. Zhang,[6] Y. Zhang,[2] Yi. Zhang,[2] Zhaxisangzhu,[5] and X. X. Zhou[7]
(The Tibet ASγ Collaboration)

Received 2007 October 30; accepted 2008 January 10

ABSTRACT

We present an updated all-particle energy spectrum of primary cosmic rays in a wide range from 10^{14} to 10^{17} eV using 5.5×10^7 events collected from 2000 November through 2004 October by the Tibet-III air-shower array located 4300 m above sea level (an atmospheric depth of 606 g cm^{-2}). The size spectrum exhibits a sharp knee at a corresponding primary energy around 4 PeV. This work uses increased statistics and new simulation calculations for the analysis. We discuss our extensive Monte Carlo calculations and the model dependencies involved in the final result, assuming interaction models QGSJET01c and SIBYLL2.1, and heavy dominant (HD) and proton dominant (PD) primary composition models. Pure proton and pure iron primary models are also examined as extreme cases. A detector simulation was also performed to improve our accuracy in determining the size of the air showers and the energy of the primary particle. We confirmed that the all-particle energy spectra obtained under various plausible model parameters are not significantly different from each other, which was the expected result given the characteristics of the experiment at high altitude, where the air showers of the primary energy around the knee reach near-maximum development, with their features dominated by electromagnetic components, leading to a weak dependence on the interaction model or the primary mass. This is the highest statistical and the best systematics-controlled measurement covering the widest energy range around the knee energy region.

Subject headings: cosmic rays — methods: data analysis — supernovae: general

Online material: color figures

1. INTRODUCTION

Although almost 100 years have passed since the discovery of cosmic rays, their source and acceleration mechanism are still not fully understood. The energy spectrum and chemical composition of cosmic rays can be key pieces of information for probing their origin, acceleration mechanism, and propagation mechanism. The cosmic-ray spectrum has been determined by many ground-based experiments to resemble two power laws, with the form $dj/dE \propto E^{-\gamma}$, where $\gamma = 2.7$ below the energy around 4×10^{15} eV, and then steepening to $\gamma = 3.1$ above this energy (Hörandel 2003). The change of the power index at this energy is called the spectral "knee." Although the existence of the knee has been well

[1] Department of Physics, Hirosaki University, Hirosaki 036-8561, Japan.
[2] Key Laboratory of Particle Astrophysics, Institute of High Energy Physics, Chinese Academy of Sciences, Beijing 100049, China.
[3] Faculty of Engineering, Yokohama National University, Yokohama 240-8501, Japan.
[4] Department of Physics, Hebei Normal University, Shijiazhuang 050016, China.
[5] Department of Mathematics and Physics, Tibet University, Lhasa 850000, China.
[6] Department of Physics, Shandong University, Jinan 250100, China.
[7] Institute of Modern Physics, Southwest Jiaotong University, Chengdu 610031, China.
[8] Department of Physics, Yunnan University, Kunming 650091, China.
[9] Faculty of Engineering, Kanagawa University, Yokohama 221-8686, Japan.
[10] Faculty of Education, Utsunomiya University, Utsunomiya 321-8505, Japan.
[11] Institute for Cosmic Ray Research, University of Tokyo, Kashiwa 277-8582, Japan.
[12] Department of Physics, Konan University, Kobe 658-8501, Japan.
[13] Research Institute for Science and Engineering, Waseda University, Tokyo 169-8555, Japan.
[14] Department of Physics, Shinshu University, Matsumoto 390-8621, Japan.
[15] Center of Space Science and Application Research, Chinese Academy of Sciences, Beijing 100080, China.
[16] Physics Department and Tsinghua Center for Astrophysics, Tsinghua University, Beijing 100084, China.
[17] Department of Physics, Saitama University, Saitama 338-8570, Japan.
[18] Advanced Media Network Center, Utsunomiya University, Utsunomiya 321-8585, Japan.
[19] National Institute of Informatics, Tokyo 101-8430, Japan.
[20] Tochigi Study Center, University of the Air, Utsunomiya 321-0943, Japan.
[21] Tokyo Metropolitan College of Industrial Technology, Tokyo 116-8523, Japan.
[22] Max-Planck-Institut für Physik, München D-80805, Germany.
[23] Shonan Institute of Technology, Fujisawa 251-8511, Japan.
[24] RIKEN, Wako 351-0198, Japan.
[25] School of General Education, Shinshu University, Matsumoto 390-8621, Japan.

established experimentally, there is still controversy as to its origin (Hörandel 2004). Proposals for its origin range from astrophysical scenarios such as a change of acceleration mechanisms (Berezhko & Ksenofontov 1999; Stanev et al. 1993; Kobayakawa et al. 2002; Völk & Zirakashvili 2004) at the sources of cosmic rays (supernova remnants, pulsars, etc.), to a single-source assumption (Erlykin & Wolfendale 2005) or effects due to propagation (Ptuskin et al. 1993; Candia et al. 2002) inside the galaxy (diffusion, drift, escape from the Galaxy), to particle physics models such as the interaction with relic neutrinos (Wigmans 2003) during transport or new processes in the atmosphere (Nikolsky & Romachin 2000) during air-shower development. Common to all models is the prediction of a change of the chemical composition over the knee region. Direct measurements of primary cosmic rays on board balloons or satellites are the best ways to study this chemical composition; however, the energy region that they can cover with sufficient statistics is limited to 10^{14} eV. The energy spectrum and chemical composition of primary cosmic rays around the knee, therefore, has to be studied with ground-based air-shower experiments using a surface array and/or detectors of Cerenkov light.

Many reports have been made on the energy spectrum, as well as the chemical composition of primary cosmic rays. Although the global features of the all-particle spectrum agree well when we take into account the systemic errors of about 20% that are involved in the energy scale (Hörandel 2003), there are still serious disagreements in the chemical composition depending on the experimental method. For example, the knee composition obtained by the Tibet and KASCADE experiments can be summarized as follows. We have already reported the energy spectrum of protons and helium in the energy range from 200 to 10,000 TeV (Amenomori et al. 2000, 2006a) from air-shower core observations, suggesting a steep power index of approximately -3.1. This indicates that the power index of the light component is changed from approximately -2.7 as measured by direct observations to -3.1 at around a few hundred TeV. Hence, the light component should become less abundant at the knee, and the main component responsible for the structure of the knee must be heavier than helium. Furthermore, the spectral shape of the light component seems to follow the power law instead of the exponential cutoff. On the other hand, KASCADE, which uses electron-muon size analysis (Antoni et al. 2005), claims that the knee in the all-particle spectrum is due to the steepening of the spectra of light elements with an exponential-type cutoff.

The accurate measurement of the all-particle energy spectrum around the knee is essential to establish the chemical composition of cosmic rays in this energy range. There is no precise measurement of the chemical composition around the knee region yet, and it is impossible to discriminate individual elements clearly by indirect observations. Therefore, most of the works published so far simply discuss the average mass $\langle \ln A \rangle$. Another approach is to unfold the all-particle spectrum using shower characteristics such as the electron-muon ratio, the depth of the shower maximum, and so on. In these methods, the detailed information of the all-particle spectrum plays an important role in determining chemical composition. It is also expected that the specific features of each component, such as cutoff energy or source characteristics, should be reflected in the shape of the all-particle spectrum, as discussed in the single-source model (Erlykin & Wolfendale 2005). The important features of the all-particle spectrum are the absolute intensity, the position of the knee, the difference of the power index before and after the knee, and the sharpness in the size spectrum, all of which are deeply connected with the acceleration mechanism and the source of cosmic rays.

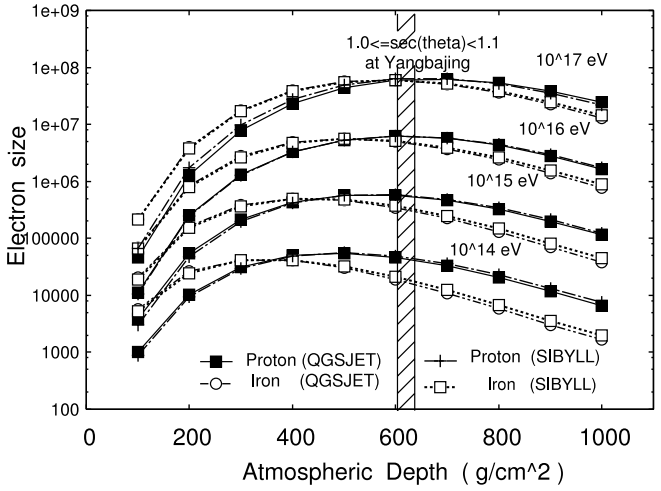

FIG. 1.—Average transition curves of air-shower size induced by protons and iron nuclei for a vertical incidence.

The merit of the air-shower experiment in Tibet is that the atmospheric depth of the experimental site (4300 m above sea level; 606 g cm^{-2}) is close to the maximum development of the air showers, with energies around the knee almost independent of the masses of primary cosmic rays, as demonstrated in Figure 1 for vertically incident cosmic rays. It should be also noted that the number of shower particles is dominated by the electromagnetic component, with a minor contribution from muons, whose interaction model dependence is known to be rather large among current interaction models, leading to a large systemic error in the experiments carried out at sea level because of the large contribution of muons. In other words, the air-shower observation at high altitude is sensitive to the most forward region of the hadronic interactions in the center-of-momentum system (CMS), where high-energy secondaries are produced, and the electromagnetic component as a decay product of neutral pions dominates the number of shower particles, while remaining insensitive to the central region of the CMS, where a large number of muons are produced as the decay product of charged pions. The differences among current interaction models are mainly related to the central region, as seen in the problem of the electron-muon correlation. Hence, the air-shower experiment in Tibet can determine the primary cosmic-ray energy with much less dependence on the chemical composition and the interaction model than experiments at sea level.

We have already reported the first result on the all-particle spectrum around the knee region based on observations from 2000 November to 2001 October by the Tibet-III air-shower array (Amenomori et al. 2003a). In this paper, we present an updated all-particle energy spectrum using the data set collected from 2000 November through 2004 October. The updates are due to (1) statistics increased approximately 2.6 times, (2) the use of new simulation codes, and (3) improvement of the lateral structure function used for the size estimation of air showers. The previous result was obtained using almost the same analysis as that used in Tibet-I (Amenomori et al. 1996), except for the parameters that depend on the detector configuration. In the present paper, the simulation code COSMOS is replaced by CORSIKA with interaction models QGSJET01c and SIBYLL2.1, a code now widely used in many analyses by other authors, which makes easier the comparison of this work with others. The third update to the structure function allows us to cover a wider energy range than before (see § 4.1.3).

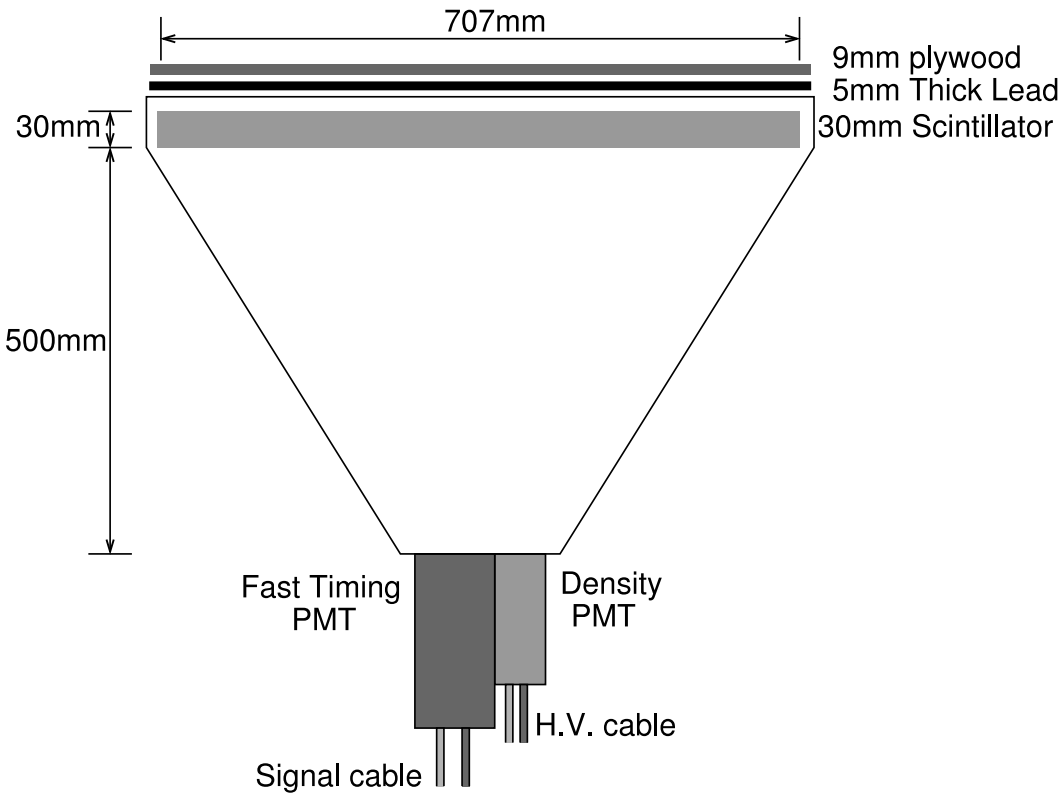

FIG. 2.—Schematic view of a detector with first timing PMT and density PMT coupling. This type of detector is labeled "FT Detector w/D-PMT" in Fig. 3. [*See the electronic edition of the Journal for a color version of this figure*.]

Thus, we obtained the all-particle energy spectrum of cosmic rays in a wide range over 3 decades between 10^{14} and 10^{17} eV, and the updated result is compared with previous ones.

2. TIBET EXPERIMENT

The Tibet air-shower experiment has been operated at Yangbajing (E 90°31′, N 30°06′; 4300 m above sea level) in Tibet, China, since 1990. The Tibet air-shower array is designed not only for observation of air showers of nuclear component origin, but also for observation of high-energy celestial gamma rays. To address these multiple purposes, the detector was constructed to cover a wide dynamic range of particle densities, covering 0.1 to 5000, and with an angular resolution able to measure to within 1° the arrival direction of air showers with energies in excess of a few TeV.

The Tibet-I surface array was constructed in 1990 (Amenomori et al. 1992) using 65 plastic scintillation detectors placed on a lattice with 15 m spacing. This array was gradually expanded to the Tibet-II (1994) and Tibet-III (1999) arrays. At present, it consists of 761 fast timing (FT) counters with 28 density (D) counters surrounding them. In the inner 36,900 m^2, FT counters are deployed at 7.5 m lattice intervals. Each of the FT counters is equipped with a fast-timing photomultiplier tube (FT-PMT; Hamamatsu H1161) that measures up to 15 particles. Among the 761 FT counters, 249 sets of detectors (with intervals of 15 m) are also equipped with density photomultiplier tubes (D-PMTs; Hamamatsu H3178) of wide dynamic range that measure up to 5000 particles in addition to the FT-PMTs, so that ultra-high-energy (UHE) cosmic rays with energy above the knee can be observed with high accuracy.

Each counter has a plastic scintillator plate (BICRON BC-408A) of 0.5 m^2 in area and 3 cm in thickness. A lead plate 0.5 cm thick is put on the top of each counter, as shown in Figure 2, in order to increase the counter's sensitivity by converting the photons in an electromagnetic shower into electron-positron pairs (Bloomer et al. 1988; Amenomori et al. 1990). The recording of signals is made for time and charge information for the FT-PMTs, but only for the charge information for the D-PMTs. The D counters surrounding the inner array are also equipped with both FT-PMTs and D-PMTs, where only the charge information of both PMTs are recorded. An event trigger signal is issued when any four-fold coincidence occurs in FT counters recording more than 0.6 particles. Figure 3 is the schematic view of the Tibet-III array.

The primary energy of each event is determined by the shower size, N_e, which is calculated by fitting the lateral particle density distribution to the modified Nishimura-Kamata-Greisen (NKG) structure function (see § 4.1.3). The air-shower direction can be estimated with an inaccuracy smaller than 0.2° at energies above 10^{14} eV, which is calibrated by observing the Moon's shadow (Amenomori et al. 2003b). We used the data set obtained from 2000 November through 2004 October. The effective live time used for the present analysis is 805.17 days.

3. SIMULATION

Monte Carlo simulations (MCs) play an important role in air-shower experiments, since most methods of analysis are developed so that they can reproduce the inputs of simulated events such as the primary energy, the location of the shower axis, the arrival direction, and so on. Even the most basic quantities, such as the number of particles arriving at a detector, should be "defined" through a MC, because we do not measure the number of particles but the charge of PMT output, which is not simply proportional to the number of charged particles entering the detector if we take into account the contributions to the electromagnetic processes by photons inside the detectors. Another example of the role of the

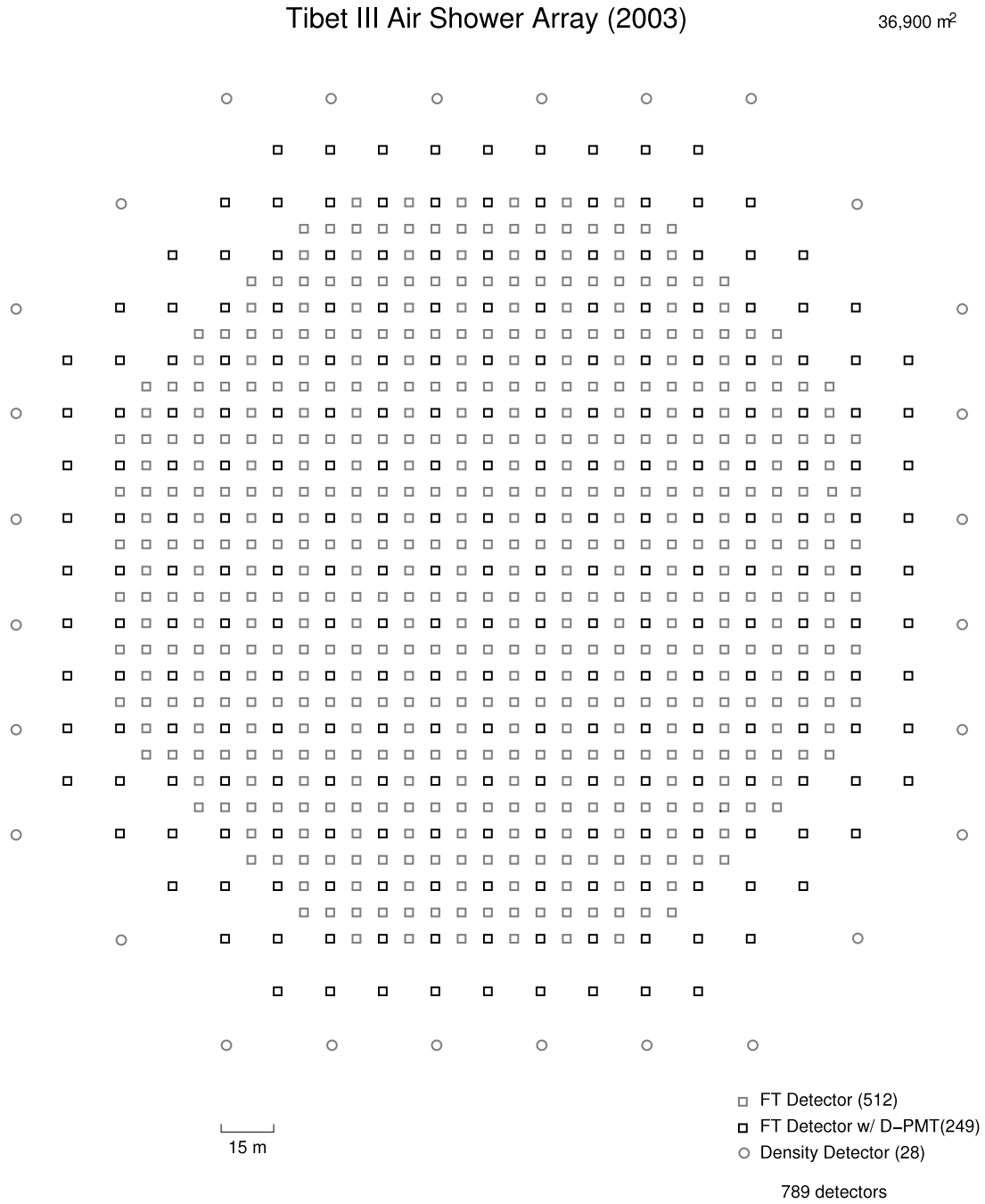

FIG. 3.—Schematic view of the Tibet-III array operating at Yangbajing. The Tibet-III array consists of 761 FT detectors and 28 D detectors around them. In the inner 36,900 m^2, FT detectors are deployed at 7.5 m lattice intervals, and 249 sets of detectors are also equipped with D-PMT, in addition to FT-PMTs. *Open gray squares*: FT detectors with FT-PMT. *Open black squares*: FT detectors with FT-PMT and D-PMT. *Open circles*: Density detectors with only D-PMT.

MC is to define the effective area of the shower array, which should be determined to avoid the erroneous counting of events whose shower axes fall outside the effective area. Therefore, detailed MC calculations are needed on air-shower generation in the atmosphere and on the detector response. Consequently, the final result inevitably depends on the interaction model and on the primary composition model in the MC. This is the main source of the systemic errors involved in the air-shower experiment, and we try to show them explicitly in the present work.

A full MC simulation has been carried out on the development of air showers in the atmosphere and also on the detector response of the Tibet-III array. The simulation code CORSIKA (ver. 6.204), which includes QGSJET01c and SIBYLL2.1 interaction models (Heck et al. 1998), is used to generate air-shower events. All shower particles in the atmosphere are traced down to the minimum energy of 1 MeV without using a thinning method.

Although the chemical composition of the primary particles around the knee region is not well established, we have to assume it in the simulation. The simplest way to bracket all possibilities is to assume pure proton and pure iron primaries. Since it is almost evident that such assumptions are not realistic and lead to unacceptable results that disagree with direct observations, these results will be mentioned as extreme cases. The chemical composition can be treated more realistically by extrapolating the known composition at low energies as measured by direct observation. The uncertainty in extrapolating to the high-energy range can be treated

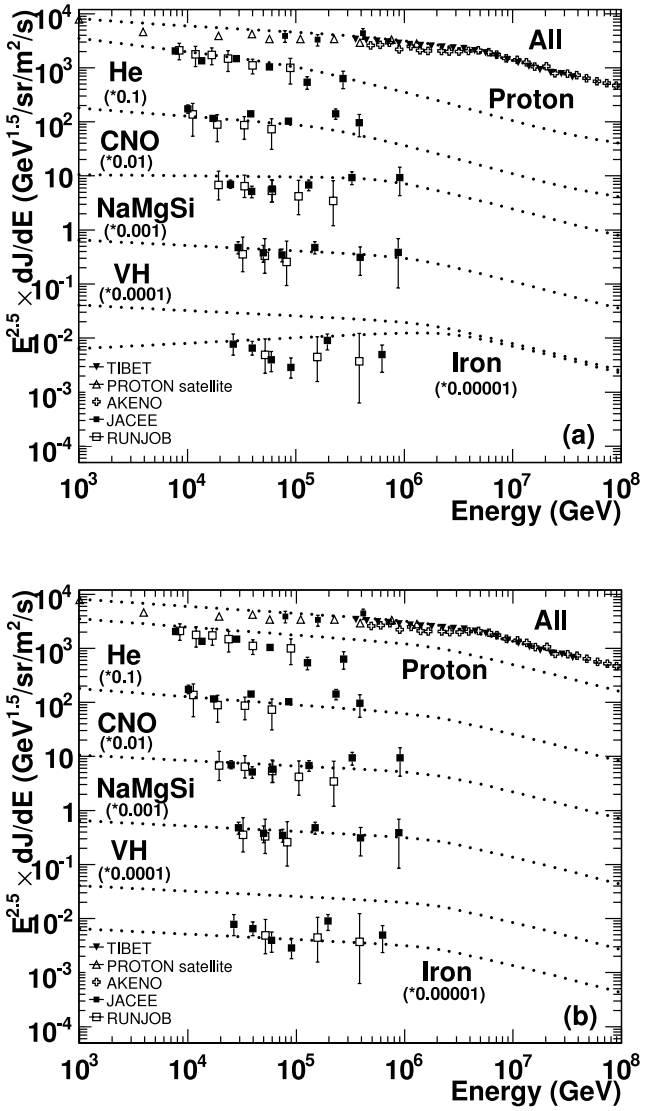

FIG. 4.—Primary cosmic-ray composition for (*a*) the HD model and (*b*) the PD model. The all-particle spectrum, which is the sum of all components, is normalized to the Tibet data and compared with other experiments: the *PROTON* satellite (Grigorov et al. 1971), AKENO (Nagano et al. 1984), JACEE (Asakimori et al. 1998), and RUNJOB (Apanasenko et al. 2001).

by bracketing the reported results on the composition study around the knee. In order to examine the composition dependence involved in the all-particle spectrum, we used two kinds of mixed-composition models. One is based on the dominance of heavy components around the knee, as reported in the literature (Amenomori et al. 2006a, 2000; Ogio 2004); this composition is called the HD model. Another is based on the dominance of light components (protons and He), also as reported in the literature (Antoni et al. 2005; Aglietta et al. 2004; Fowler et al. 2001); this composition is called the PD model. The energy spectra of the individual mass groups in the HD and PD models are shown in Figures 4*a* and 4*b*, respectively. Table 1 shows their fractional contents at given energies. In total, four kinds of primary compositions, namely, pure proton, pure iron, the HD model, and the PD model, are used in the simulation with a minimum primary energy of 50 TeV.

All secondary particles are traced until their energies become 1 MeV in the atmosphere. The shower axis was placed on the Tibet array at random within a radius of 100 m from the center of the array. In order to treat the MC events in the same way as experimental data analysis, simulated air-shower events were input to the detector with the same detector configuration as the Tibet-III array, and the Epics code (ver. 8.64)[26] was used to calculate the energy deposit of these shower particles. Experimentally, the number of charged particles is defined as the PMT output (charge) divided by that of the single-particle peak, which is determined by a probe calibration using cosmic rays, typically single muons. For this purpose, a small scintillator 25 cm × 25 cm × 3.5 cm thick with a PMT (H1949) is put on the top of each detector during the maintenance period. This is called a probe detector and is used for making the trigger of each Tibet-III detector. The response of each detector is calibrated every year through probe calibration. In the simulation, the events triggered by the probe detector were also examined by a MC calculation in which the primary particles were sampled in the energy range above the geomagnetic cutoff energy at Yangbajing (>10 GeV), and all secondary particles that passed the probe detector and the Tibet-III detector simultaneously were selected for the analysis. Since the value of PMT output is proportional to the energy loss of the particles passing through the scintillator, the peak position of the energy loss distribution corresponds to the experimental single peak of the probe calibration.

According to the MC, the peak position of the energy loss in the scintillator is 6.11 MeV (for details, see in Amenomori et al. 2007). We then calculated the number of charged particles for each detector hit as the total energy loss in each scintillator divided by 6.11 MeV, instead of counting the number of charged particles arriving at the detector in MC events. We confirmed that the shape of the energy loss distribution, which is determined by probe calibration simulation, shows a reasonable agreement with the charge distribution of the experimental data, as shown in Figure 5, where the proportionality between the energy loss ΔE and the PMT output charge Q_i is assumed to be $Q_i = k_i \times \Delta E$, where k_i is a proportional constant, which, depending on the detector, is typically around 4 pico-Coulombs MeV^{-1}. Thus, all detector responses, including muons and the materialization of photons inside the detector, are taken into account. The total number of charged particles of each event (the shower size N_e) was estimated using the modified NKG lateral distribution function, which is tuned

TABLE 1

FRACTIONS OF COMPONENTS IN THE ASSUMED PRIMARY COSMIC-RAY SPECTRUM OF THE HD AND PD MODELS

Component	10^{14}–10^{15} eV (%)	10^{15}–10^{16} eV (%)	10^{16}–10^{17} eV (%)
HD Model			
Proton	22.6	11.0	8.1
He	19.2	11.4	8.4
Medium (CNO)	21.0	22.6	17.8
Heavy (NaMgSi)	9.0	9.4	8.1
Very heavy (SClAr)	5.6	6.2	5.8
Fe	22.2	39.1	51.7
PD Model			
Proton	39.0	38.1	37.5
He	20.4	19.4	19.1
Medium (CNO)	15.2	16.1	16.5
Heavy (NaMgSi)	9.4	9.9	10.2
Very heavy (SClAr)	5.8	6.2	6.3
Fe	9.4	9.9	10.2

NOTE.—Fractions from Amenomori et al. (2000).

[26] See http://cosmos.n.kanagawa-u.ac.jp/EPICSHome/index.html.

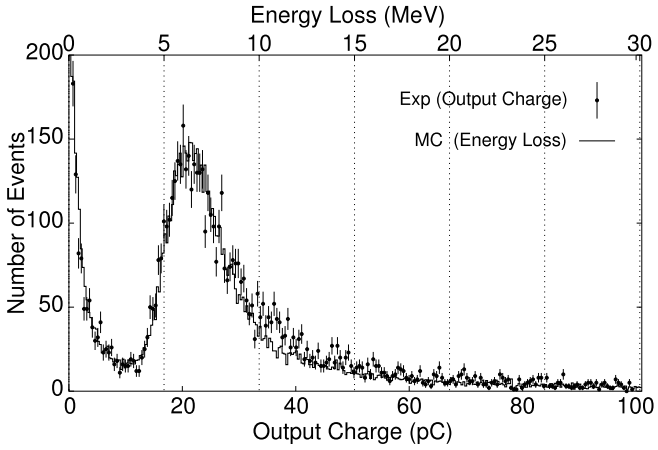

FIG. 5.—Charge distribution in a detector measured by probe calibration (see the text). In order to compare the charge distribution with the simulation of the energy loss in a scintillator, the MC result is adjusted by multiplying a constant to meet with the same peak position as the experiment. The fluctuation of the number of photons in scintillation light is taken into account with the normal distribution in MC.

to reproduce the above-defined number of particles using the MC simulation under our detector configurations. The number of typical MC events for QGSJET+HD is as follows. About 10 million air showers are generated with primary energies above 50 TeV. After imposing the selection criteria described in § 4.2, the surviving number of events is about 5 million, among which 1.9 million events belong to the unbiased energy region corresponding to $E_0 > 100$ TeV. Almost the same number of MC events are obtained for other models, which facilitates comparison.

4. ANALYSIS

4.1. *Reconstruction of Air Showers*

An example of the shower profile obtained by the Tibet-III array is shown in Figures 6*a* and 6*b*, which represent the map of arrival time and particle density of shower particles, respectively. Although the Tibet array has quite a low energy threshold (a few TeV) for the purpose of celestial gamma-ray observation, its detection efficiency for the nuclear component, including iron nuclei, is not sufficient in the low-energy region. An additional event selection condition is required for the unbiased detection of all particles and for the capability of the lateral density fitting. The following condition was applied to the selection of the events for the all-particle spectrum analysis:

$$N_D \geq 10 \text{ with } n_p \geq 5, \tag{1}$$

where N_D is the number of detectors hit, and n_p is the number of particles per detector. This condition satisfies the requirements for unbiased analysis in the energy range above 100 TeV, as described below.

4.1.1. *Determination of the Core Position*

The core position of each air shower ($X_{\rm core}$, $Y_{\rm core}$) is estimated using the following equation:

$$(X_{\rm core}, Y_{\rm core}) = \left(\frac{\Sigma\rho_i^w x_i}{\Sigma\rho_i^w}, \frac{\Sigma\rho_i^w y_i}{\Sigma\rho_i^w}\right), \tag{2}$$

where ρ_i is the particle density at the ith detector, and the weight w is an energy-dependent parameter that varies between 0.8 and 2.0. It is confirmed that the mean error of the core position can be estimated as 5 m by reconstructing MC events (see Fig. 7). A lower energy event selection condition than equation (1) leads to poorer core resolution, which makes lateral density fitting difficult.

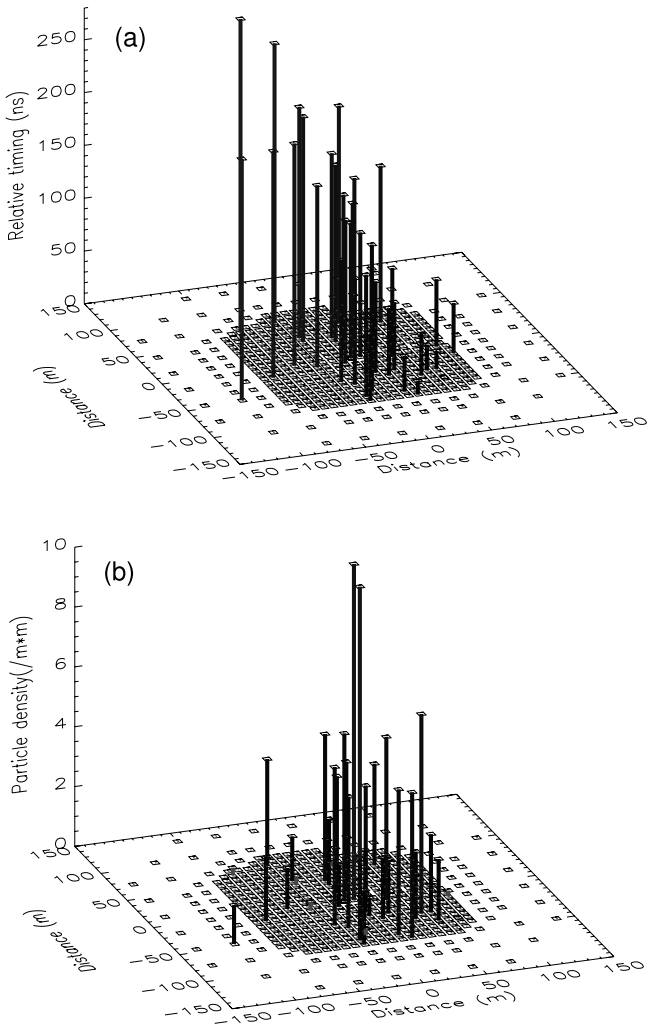

FIG. 6.—Example of the map of (*a*) arrival time of shower particles and (*b*) particle density, obtained by the Tibet-III array.

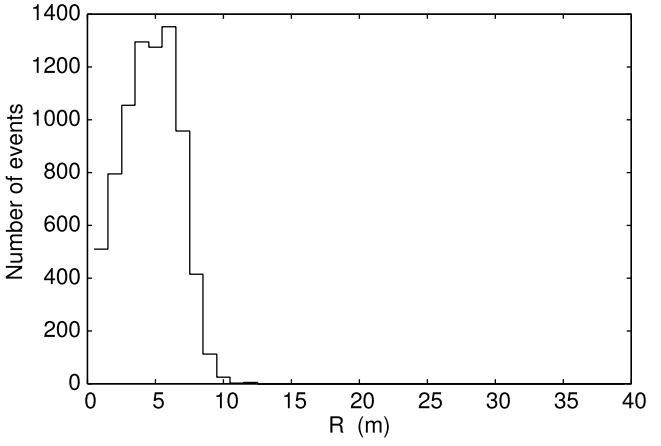

FIG. 7.—Distribution of core position error. The mean error of core position can be estimated as 5 m. Shower selection criteria are $E_0 \geq 100$ TeV, $\sec\theta \leq 1.1$, and a core position located at the inner 135 m × 135 m of the array.

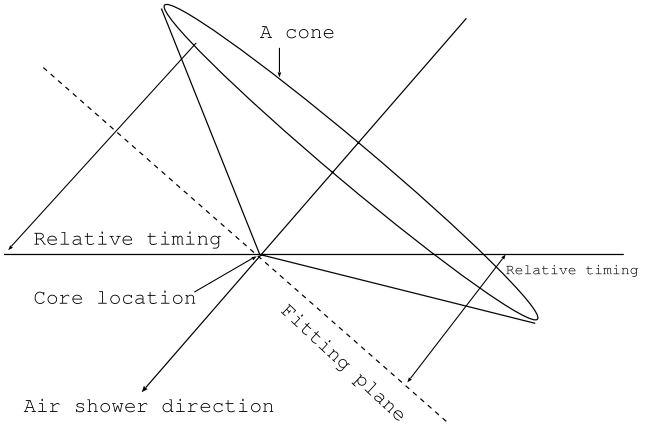

FIG. 8.—Determination of air-shower direction.

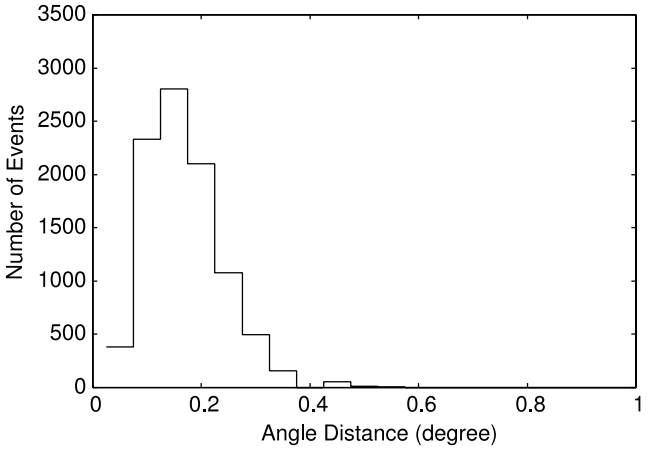

FIG. 9.—Distribution of the opening angle between true and estimated arrival directions. The mean error of the air-shower direction can be estimated as 0.2°. Shower selection criteria are $E_0 \geq 100$ TeV, $\sec\theta \leq 1.1$, and a core position located at the inner 135 m × 135 m of the array.

4.1.2. *Determination of the Arrival Direction*

The arrival direction of the air shower is estimated using the time signal measured by the 761 FT (fast-timing) counters. The shape of the shower front is assumed to be a reverse-conic type, as shown in Figure 8. The direction cosine of the shower axis is determined by using a method of least squares in which the difference is minimized between the arrival time signals of each detector and the expected values on the assumed cone with the given direction cosine.

An experimental check of the angular resolution by this method is made by observation of the Moon's shadow (Amenomori et al. 2003b) using large statistics of low-energy events (>3 TeV) and also a so-called even-odd method, which many authors have used for estimating the angular resolution (Amenomori et al. 1990). The reconstruction of the high-energy MC events assures us that the mean error of the air-shower direction can be estimated as 0.2° at energies above 10^{14} eV (see Fig. 9).

4.1.3. *Estimation of the Shower Size*

The lateral density distribution is corrected to the inclined plane perpendicular to the shower axis and used for the shower size estimation. In this work, the determination of the lateral distribution function of shower particles is very important, since the total number of charged particles in each event is estimated by fitting this function to the experimental data. Using the MC data obtained under the same conditions as the experiment, we found that the following modified NKG function can be well fitted to the lateral distribution of shower particles under a lead plate of 5 mm thickness:

$$f(r,s) = \frac{N_e}{C(s)} \left(\frac{r}{r'_m}\right)^{a(s)} \left(1 + \frac{r}{r'_m}\right)^{b(s)} \Big/ r'^2_m, \tag{3}$$

$$C(s) = 2\pi B[a(s) + 2, -b(s) - a(s) - 2], \tag{4}$$

where $r'_m = 30$ m, s corresponds to the age parameter, N_e is the total number of shower particles, and B denotes the beta function. The original meaning of r_m in the NKG formula is a Moliere unit, which is 130 m at Tibet altitude; however, we treat r'_m as a unit scale of the lateral distribution suitable to describe the structure of the air showers observed by the Tibet-III array, whose effective area is 135 m × 135 m. The functions $a(s)$ and $b(s)$ are determined as follows. In the CORSIKA simulation, the shower age parameter s is calculated at observation level by fitting the number of particles to a function for the one-dimensional shower development. It may be possible to assume that air showers with the same shower age s are in almost the same stage of air-shower development in the atmosphere; i.e., they show almost the same lateral distribution for shower particles, irrespective of their primary energies. The lateral distribution of the particle density obtained by the simulation with carpet array configuration is normalized by the total number of particles, which is derived from the total energy deposit in an infinitely wide scintillator. These events are then classified according to the stage of air-shower development using the age parameter and averaged over the classified events. The fitting of equation (3) to the averaged MC data is done to obtain the numerical values a and b. Thus, we can obtain the behavior of a and b as a function of s, as shown in Figures 10*a* and 10*b*, where the original definitions of $a(s)$ and $b(s)$ in the NKG function are shown by dotted lines. Although our result shows dependencies of a and b on s that differ from the original NKG function, it is confirmed that the lateral distribution of the shower particles is better reproduced by our formula (see Fig. 11). This expression is valid in the range $s \simeq 0.6$–1.6, $\sec\theta < 1.1$, and $r \simeq 5$–3000 m. Two interaction models (QGSJET01c and SIBYLL2.1) and four primary composition models (pure proton, pure iron, HD, and PD) are used independently to determine the functions $a(s)$ and $b(s)$ and are used in the analysis described below. Other details are described in Amenomori et al. (2007).

Based on the MC simulation, the correlation between the true shower size (true size) and the estimated shower size (fit size) is demonstrated in Figures 12*a* and 12*b*. Here, the true shower size means the number of particles calculated for a carpet array, while the estimated shower size is for the real Tibet-III array using the modified NKG function mentioned above. As seen in these two figures, a good correlation is obtained between the true shower size and the estimated shower size. The systemic deviation of less than 1% around 100 TeV (Figure 12*a*) shows that we need finer tuning of the modified NKG function at low energies; this error was treated as a known systemic error in our analysis and was finally corrected by reducing the estimated size using the known factor from Fig.12*a*. The shower size is well reproduced with a standard deviation of 5% around the primary energy of 1000 TeV and $1.0 < \sec\theta \leq 1.1$ based on the QGSJET+HD model. The estimated shower size resolutions are summarized for the events with different simulation model combinations in Table 2.

4.2. *Data Selection*

The following event selection criteria are adopted in the present analysis. (1) More than 10 detectors should detect a signal of

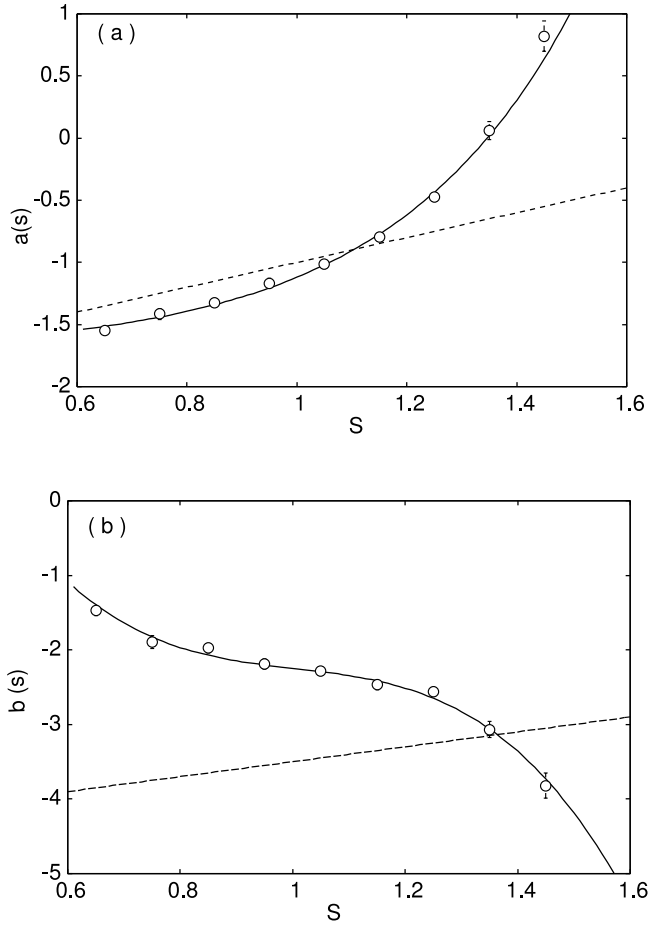

FIG. 10.—Numerical values of a (*top*) and b (*bottom*) plotted as a function of s, where the original definitions of $a(s)$ and $b(s)$ in the NKG function are shown by the dotted lines, and the open circles denote the averaged MC data using the QGSJET01c+HD model. The data are fitted by empirical formulae shown by the solid lines. See the text. [*See the electronic edition of the Journal for a color version of this figure*.]

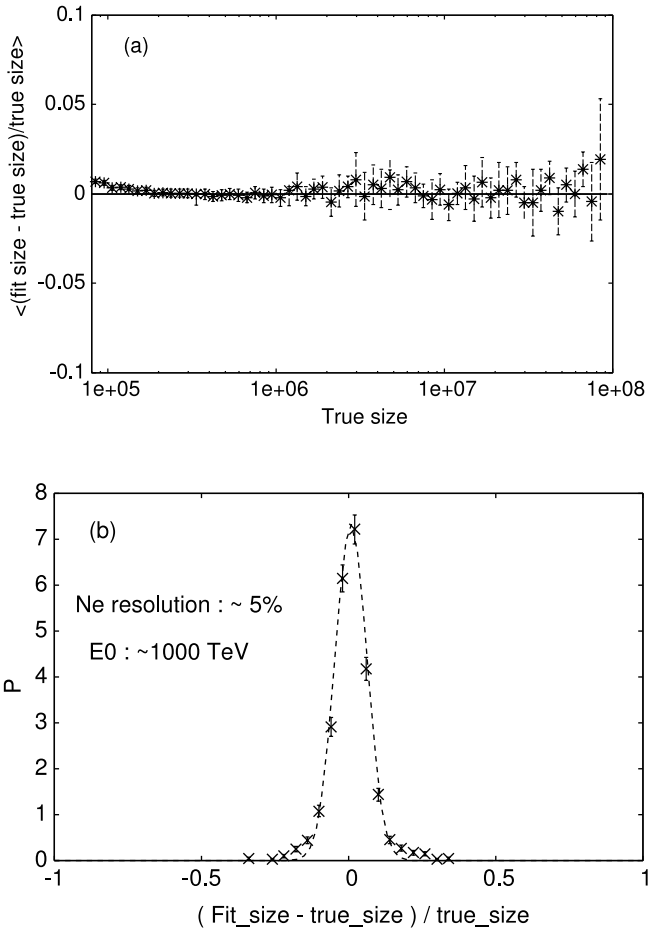

FIG. 12.—(*a*) Correlation between the true shower size and the estimated shower size (fit size). (*b*) Shower size resolution is estimated to be 5% around the primary energy of 1000 TeV based on the QGSJET+HD model. Shower selection criteria are $E_0 \geq 100$ TeV, $\sec\theta \leq 1.1$, and a core position located at the inner 135 m $\times$ 135 m of the array.

more than 5 particles per detector, as mentioned in equation (1). (2) In order to minimize the primary mass dependence on the air-shower size at Yangbajing altitude, the zenith angle, θ, of the arrival direction of air showers should be smaller than 25°, or $\sec\theta \leq 1.1$. (3) The rejection of the events falling outside the effective area of the array should be made by estimating the core position using equation (2), with a high weight of $w = 8.0$ for the particle density. Then, we impose the condition that the core position should be inside the innermost 135 m $\times$ 135 m of area (18,225 m^2). This area is chosen by using MC events, so that the following two cases cancel each other out; namely, the number of events that originally fall inside this area but that fall outside after event reconstruction should equal the number of events in the opposite case. This is confirmed by simulations showing that out-in events occupy about 10% of all selected events (see Fig. 13), and that the energy spectra of out-in and in-out events are almost the same; hence, the effect of the difference between them and all selected events is less than 2% in each energy bin.

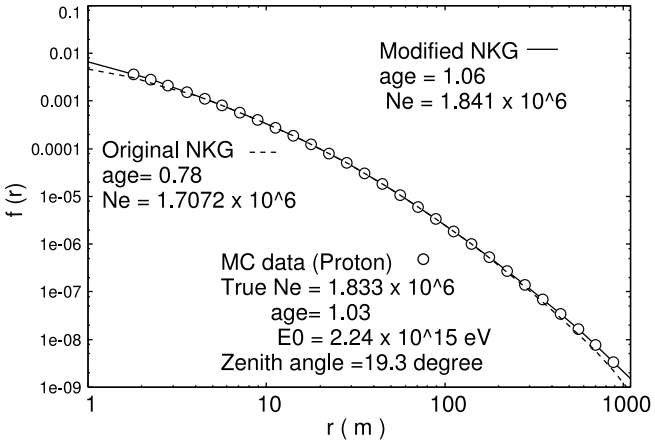

FIG. 11.—Lateral density distribution of the charged particles obtained with use of the carpet simulation. The shower size N_e is better reproduced by our modified NKG function.

TABLE 2
SHOWER SIZE RESOLUTION

E_0	QGSJET+HD (%)	QGSJET+PD (%)	SIBYLL+HD (%)	SIBYLL+PD (%)
100 TeV	9.0	9.1	9.2	9.5
1000 TeV	5.0	5.8	5.2	5.9

NOTE.—Summarized for the events induced by primary particles of $E_0 \simeq 100$ TeV and $E_0 \simeq 1000$ TeV, with $\sec\theta \leq 1.1$ and the core position located at the inner 135 m $\times$ 135 m of the array, for the QGSJET+HD, QGSJET+PD, SIBYLL+HD and SIBYLL+PD models.

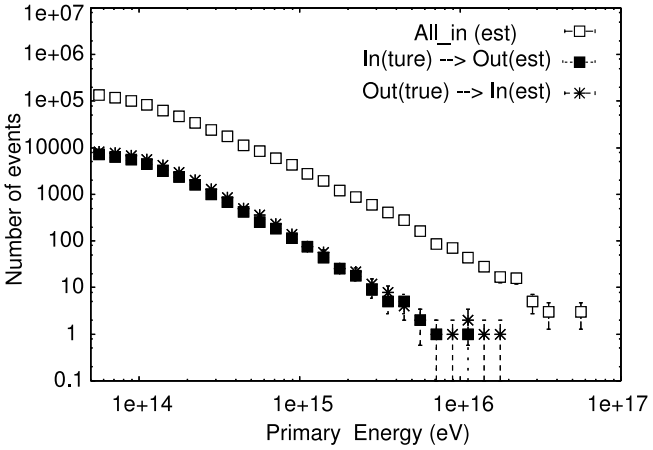

FIG. 13.—Out-in events occupy about 10% of all selected events. The energy spectrum of out-in and in-out events are almost the same, as the effect of the difference between them in all selected events is less than 2% at each energy bin.

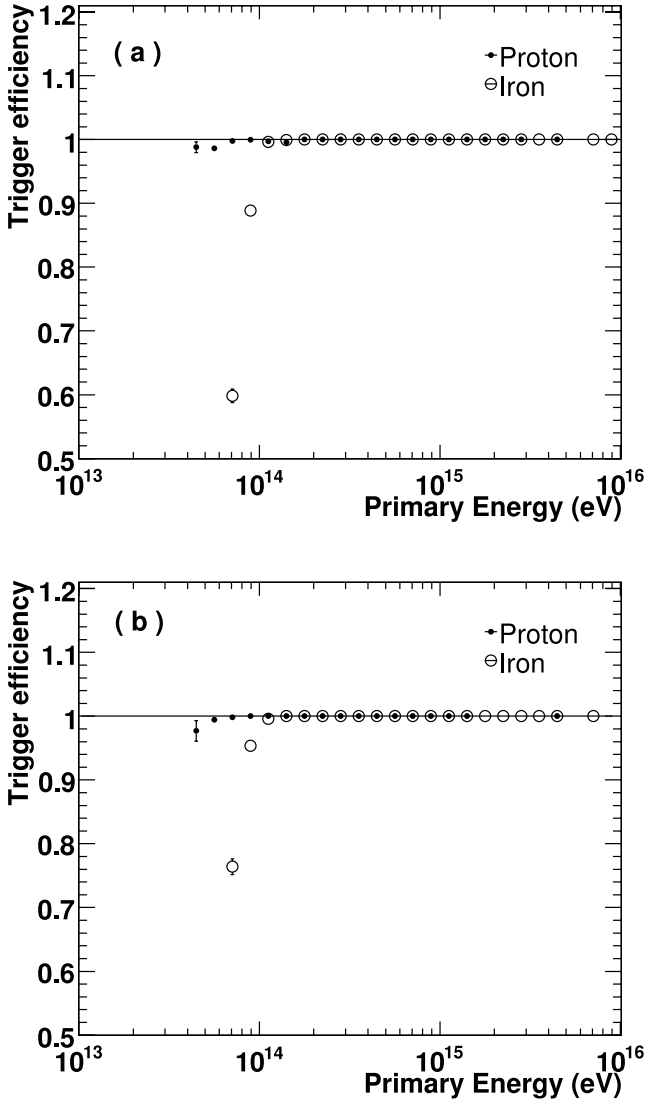

FIG. 14.—Trigger efficiency of air showers. In the case of $N_D \geq 10$, $n_p \geq 5$, and $\sec\theta \leq 1.1$ with the core position located at the inner 135 m × 135 m of the array, the air showers induced by protons or iron with $E_0 \geq 100$ TeV can be fully detected without any bias. (*a*) QGSJET. (*b*) SIBYLL.

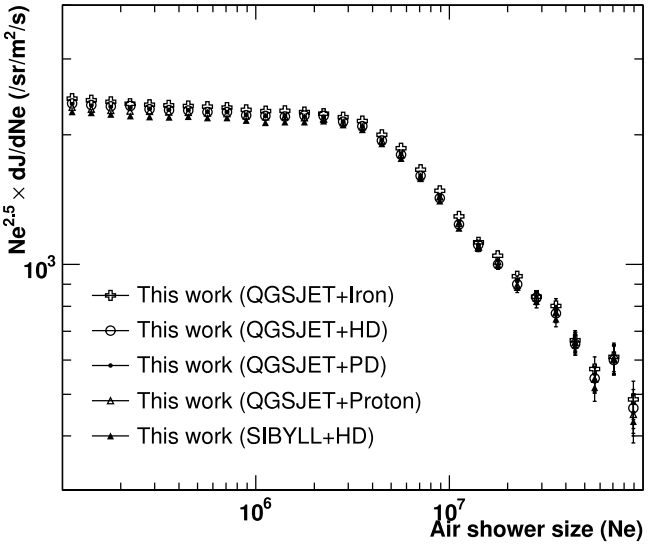

FIG. 15.—Model dependence of the size spectrum of nearly vertical air showers ($\sec\theta \leq 1.1$).

4.3. *Trigger Efficiency*

Our simulations confirmed that the air showers induced by primary particles with $E_0 \geq 100$ TeV can be fully detected without any bias under the above-mentioned criteria, as shown in Figure 14. The total effective area $S \times \Omega$ is then calculated to be 10,410 m^2 sr for all primary particles with $E_0 \geq 100$ TeV using an inner area of 135 m × 135 m and a solid angle with $\sec\theta \leq 1.1$. For the calculation of the absolute intensity, the inclination effect due to a flat surface detector is taken into account by correcting the density of the observed events into that for a plane perpendicular to the shower axis. For the operation period from 2000 November through 2004 October, the effective live time T is calculated as 805.17 days. The total number of air showers selected under the above conditions is 5.5×10^7 after the inclination correction.

5. RESULTS AND DISCUSSIONS

5.1. *Model Dependence of the Size Spectrum*

As a first step in checking the model dependence, the difference of the size spectra derived by the lateral fitting is examined using structure functions based on five models (the QGSJET interaction

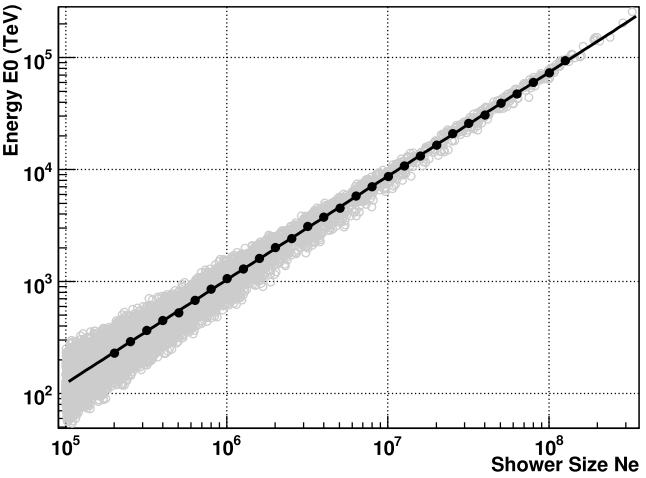

FIG. 16.—Scatter plots of the primary energy E_0 and the estimated shower size N_e based on the QGSJET+HD model.

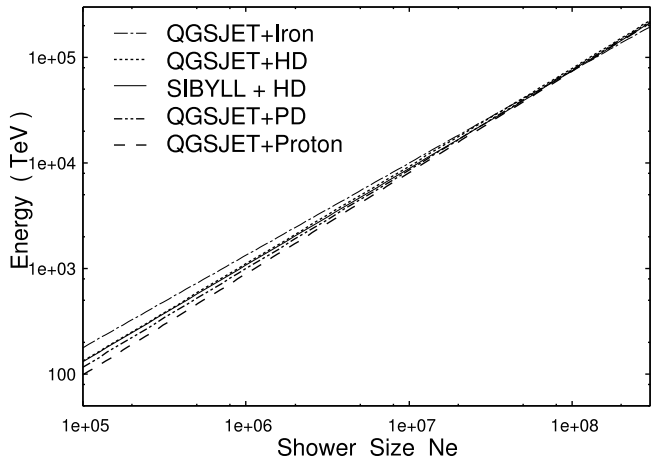

FIG. 17.—Correlations between the estimated shower size N_e and the primary energy E_0 for given models.

model with four primary composition models and the SIBYLL+HD model). Shown in Figure 15 is the model dependence of the air-shower size spectrum of nearly vertical air showers. It is seen that the model dependence of the air-shower size is small (less than 5% in absolute intensity on the primary composition model, and also less than 5% on the hadronic interaction models).

5.2. *All-Particle Energy Spectrum*

5.2.1. *Determination of the Primary Energy*

In Figure 16, we show the scatter plots of the primary energy E_0 and the estimated shower size N_e based on the QGSJET+HD model. Figure 17 shows the correlations between the estimated shower size N_e and the primary energy E_0 for QGSJET+4 primary models and the SIBYLL+HD model. In this figure, the results of the pure composition models are also shown to help the understanding of the composition dependence in the energy determination. Using these pure composition models will result in remarkably different primary energy spectra, as shown later. The correlation between the estimated shower size N_e and the primary energy E_0 for $\sec\theta \leq 1.1$ can be well fitted using the following conversion function for each interaction model and composition model:

$$E_0 = a\left(\frac{N_e}{1000}\right)^b \text{ TeV}, \tag{5}$$

where the numerical values of a and b in equation (5) are summarized in Table 3. These approximations are valid for nearly vertical air showers ($\sec\theta \leq 1.1$) at Yangbajing altitude.

As seen in Figure 17, the difference in the conversion factor between the two mixed-composition models of HD and PD is not significant and almost disappears above a few $\times$ 1000 TeV in spite of the large difference in the fractional abundances of the chemical components. From the comparison between QGSJET+HD and SIBYLL+HD, one can see that the dependence on the interaction model is very small.

It is also noted that the energy resolutions in different interaction models and the two mixed-composition models are very close to each other. For the QGSJET+HD model, the differences are estimated as 36% and 17% at energies around 200 and 2000 TeV, respectively. The corresponding values for the SIBYLL+HD model are 38% and 19%, and for the QGSJET+PD model they are 39% and 19%. It is commonly understood that there is an energy-dependent flux overestimation problem due to the steep power index of the cosmic-ray energy spectrum when the error of the estimated energy increases with decreasing primary energy. It may be worthwhile, however, to note that this effect is already included in our method of determining the energy using the conversion function, because our determination of the primary energy at a given shower size includes the contribution of all possible primary energies, which leads to a smaller value than in the case without fluctuation, which reflects a larger population of low-energy primaries than high-energy ones. To avoid methodical systemic error, the reproducibility of the primary flux was carefully examined using MC events, and no significant deviation was found between the MC input spectrum and the reconstructed spectrum.

TABLE 3

PARAMETERS IN THE CONVERSION FUNCTION (EQ. [5])

	$E_0 < 10^{16}$ eV		$E_0 > 10^{16}$ eV	
MODEL	a	b	a	b
QGSJET+Proton	1.195	0.959	1.195	0.959
QGSJET+HD	1.872	0.924	1.348	0.953
QGSJET+PD	1.583	0.933	1.348	0.951
SIBYLL +HD	1.968	0.913	1.323	0.951
QGSJET+Iron	3.915	0.851	3.915	0.851

5.2.2. *Energy Spectrum of All-Particles and the Knee Parameters*

The all-particle energy spectrum of primary cosmic rays in a wide range over 3 decades between 1×10^{14} and 1×10^{17} eV is shown in Figure 18 for five models. In this figure, it is important to note that the position of the knee is clearly seen at the energy around 4 PeV, irrespective of the model used.

The model dependence of the conversion function shown in Figure 17 may lead to different shapes of the all-particle energy spectrum. The model dependence on the primary composition can be checked by comparing the results of QGSJET+HD and QGSJET+PD. Although the composition is fairly different between the HD and PD models at energies above 10^{15} eV, the difference in the absolute intensity is 20% at most between the two models and decreases with increasing primary energy. As mentioned above, it may be helpful to show the composition dependence by the pure component assumption. The difference between the pure proton and pure iron primary models becomes large in the lower energy region of the range shown in this figure, where the difference in the intensities between the two models exceeds a factor of 3 at 10^{14} eV, although we do not claim that these results reflect reality, at least in an energy range lower than a few $\times$ 10^{14} eV. It should be noted that the mixed-composition models yield a more realistic extension of direct observations, and the composition model dependence almost disappears above 10^{16} eV. This is the remarkable characteristic of the Tibet experiment.

The interaction model dependence is seen by comparing the results of the QGSJET+HD and SIBYLL+HD models. This comparison shows that the shapes of the spectrum from both interaction models are almost the same, and the difference in the absolute intensity is within 10%. In Figure 19, we show the results using the mixed-composition model compared to other works, including our previous work presented in Amenomori et al. (2003a). Figure 20 shows the higher energy region above the knee in comparison to the surface array experiments done at the highest energy region. It is very interesting to see how the extension of our spectrum above 10^{16} eV connects smoothly with the data at the highest energy region.

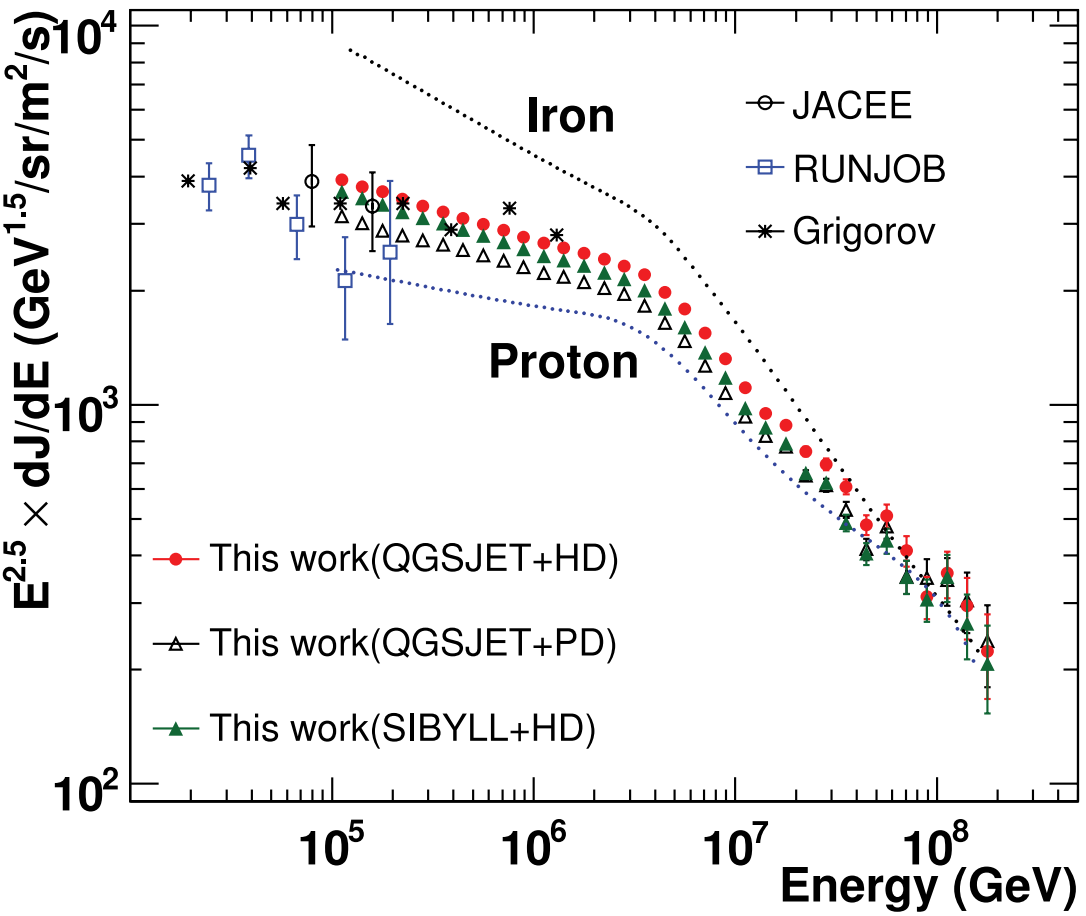

FIG. 18.—Differential energy spectra of all particles obtained by the present work using five models and compared with direct observations: JACEE (Asakimori et al. 1998), RUNJOB (Apanasenko et al. 2001), and Grigorov (Grigorov et al. 1971).

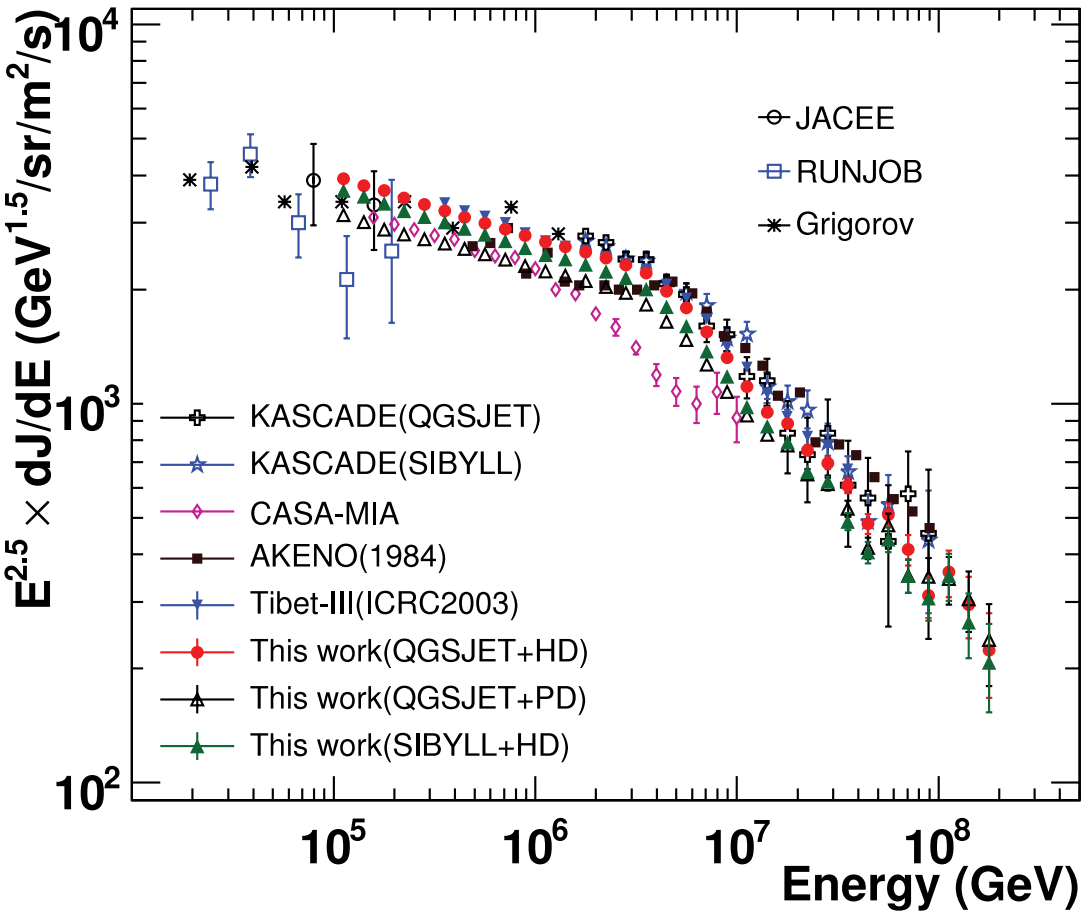

FIG. 19.—Differential energy spectra of all particles obtained by the present work using mixed-composition models compared with other experiments: JACEE (Asakimori et al. 1998), RUNJOB (Apanasenko et al. 2001), Grigorov (Grigorov et al. 1971), KASCADE (Antoni et al. 2005), CASA-MIA (Glasmacher et al. 1999), AKENO (1984) (Nagano et al. 1984), and Tibet-III (Amenomori et al. 2003a).

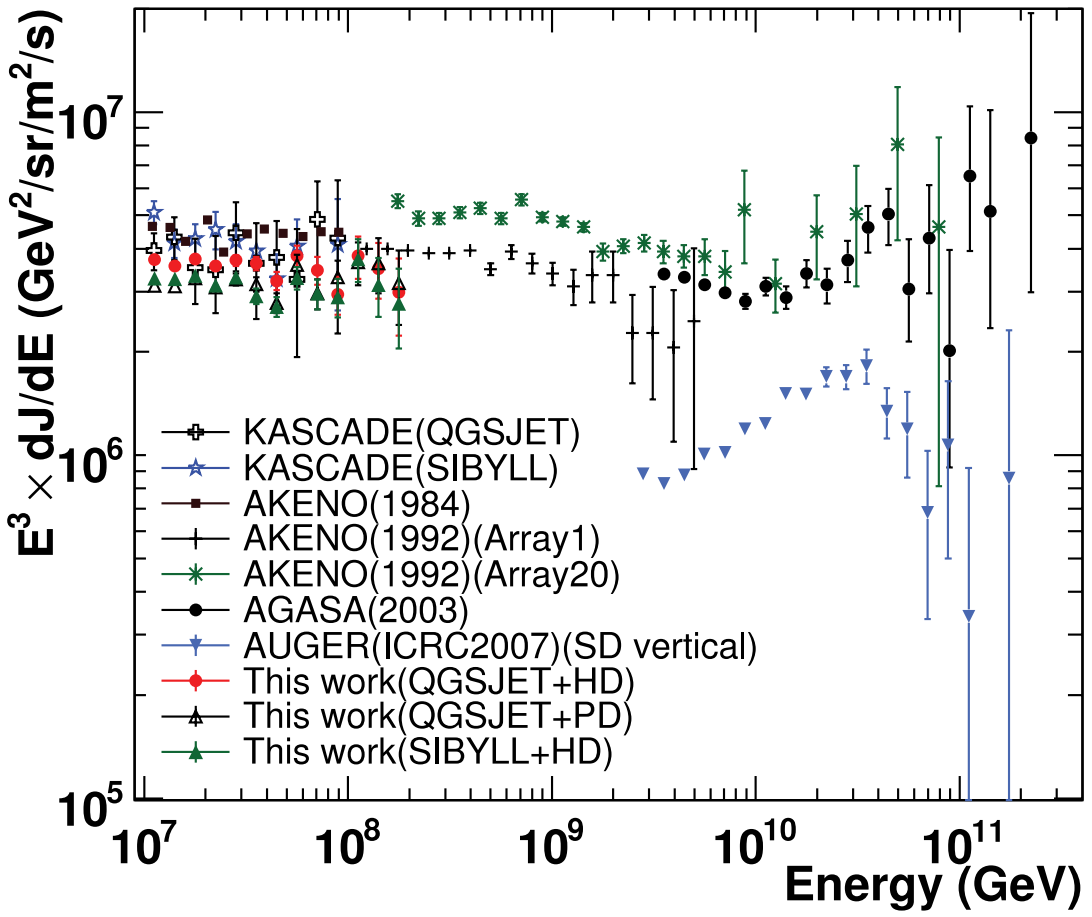

FIG. 20.—Differential energy spectra of all particles obtained by the present work above the knee compared with other experiments at the highest energy range: KASCADE (Antoni et al. 2005), AKENO (1984) (Nagano et al. 1984), AKENO (1992) (Nagano et al. 1992), AGASA(2003) (Takeda et al. 2003), AUGER (SD vertical) (Yamamoto 2007; Roth 2007)

The intensities of all-particle energy spectra measured by the Tibet-III array are also posted in Table 4, and the summary of the measured all-particle energy spectrum and knee parameters are listed in Table 5, where γ_1 is the best-fitted index for the energy range 100 TeV $< E_0 <$ 1 PeV, and γ_2 is for the energy above 4 PeV.

6. SUMMARY

We have analyzed the air-shower data set collected from 2000 November through 2004 October with the Tibet-III air-shower array using the new simulation code CORSIKA, and obtained the all-particle energy spectrum of primary cosmic rays in a wide energy range between 10^{14} and 10^{17} eV over 3 decades. The knee of the primary spectrum is clearly observed, and its position is located at around 4 PeV. This is the highest statistical and the best systematics-controlled measurement covering the widest energy range around the knee energy region.

The advantage of the Tibet experiment at high altitude is first that the primary energy for the unbiased detection of air showers is sufficiently low for the purpose of the measurement around the knee, and second that the energy determination is insensitive to the number of muons, which is dependent on the hadronic interaction model and the chemical composition. In order to quantitatively confirm these characteristics, the model dependence on the primary chemical composition was estimated in terms of the two mixed chemical composition models of HD (heavy dominant) and PD (proton dominant), which are extrapolated from direct observations with different combinations of the fractional contents of the individual elements, together with the extreme cases of pure proton and pure iron. The interaction model dependence was discussed using the QGSJET01c and SIBYLL2.1 interaction models, as they are widely used in other works. It was shown that the air showers induced by primary energies above 100 TeV are fully detected for all kinds of primary particles. The systemic errors due to the above-mentioned model dependences are shown to be within a few tens of percent in the energy range below the knee, namely 20% in chemical composition models between HD and PD, and 10% in interaction models between QGSJET01c and SIBYLL2.1. The model dependence decreases with increasing primary energy, and it almost disappears above 10^{16} eV. Although these estimates are limited for the chosen models, another choice of more adequate models, if any exist, will not drastically change the result of this work because of the weak dependence on the model used. The uncertainty due to the interaction model will even decrease after the measurement of the CMS forward region by the forthcoming Large Hadron Collider forward (LHCf) experiment (Bonechi et al. 2006; Sako et al. 2007).

As discussed above, the main uncertainty remaining in the all-particle spectrum is related to the chemical composition. This work will be extended to the analysis of air showers with large arrival zenith angles, which can show other features of air-shower development in the atmosphere and provide information about their chemical composition (to be published elsewhere). As mentioned before, we have already reported on proton and helium spectra around the

TABLE 4
INTENSITY OF ALL-PARTICLE ENERGY SPECTRUM MEASURED BY TIBET-III ARRAY FOR THE QGSJET+HD, QGSJET+PD, AND SIBYLL+HD MODELS

Energy (GeV)	$dJ/dE \pm$ stat. errors (m^{-2} s^{-1} sr^{-1} GeV^{-1})		
	QGSJET+HD	QGSJET+PD	SIBYLL+HD
1.12×10^5	$(9.300 \pm 0.002) \times 10^{-10}$	$(7.454 \pm 0.002) \times 10^{-10}$	$(8.639 \pm 0.002) \times 10^{-10}$
1.41×10^5	$(5.008 \pm 0.001) \times 10^{-10}$	$(4.013 \pm 0.001) \times 10^{-10}$	$(4.684 \pm 0.001) \times 10^{-10}$
1.78×10^5	$(2.732 \pm 0.001) \times 10^{-10}$	$(2.155 \pm 0.001) \times 10^{-10}$	$(2.529 \pm 0.001) \times 10^{-10}$
2.24×10^5	$(1.470 \pm 0.001) \times 10^{-10}$	$(1.177 \pm 0.001) \times 10^{-10}$	$(1.360 \pm 0.001) \times 10^{-10}$
2.82×10^5	$(7.934 \pm 0.004) \times 10^{-11}$	$(6.437 \pm 0.004) \times 10^{-11}$	$(7.370 \pm 0.004) \times 10^{-11}$
3.55×10^5	$(4.296 \pm 0.003) \times 10^{-11}$	$(3.522 \pm 0.002) \times 10^{-11}$	$(4.015 \pm 0.003) \times 10^{-11}$
4.47×10^5	$(2.323 \pm 0.002) \times 10^{-11}$	$(1.919 \pm 0.002) \times 10^{-11}$	$(2.173 \pm 0.002) \times 10^{-11}$
5.62×10^5	$(1.262 \pm 0.001) \times 10^{-11}$	$(1.045 \pm 0.001) \times 10^{-11}$	$(1.179 \pm 0.001) \times 10^{-11}$
7.08×10^5	$(6.834 \pm 0.008) \times 10^{-12}$	$(5.678 \pm 0.007) \times 10^{-12}$	$(6.373 \pm 0.007) \times 10^{-12}$
8.91×10^5	$(3.695 \pm 0.005) \times 10^{-12}$	$(3.071 \pm 0.005) \times 10^{-12}$	$(3.433 \pm 0.005) \times 10^{-12}$
1.12×10^6	$(2.001 \pm 0.003) \times 10^{-12}$	$(1.671 \pm 0.003) \times 10^{-12}$	$(1.853 \pm 0.003) \times 10^{-12}$
1.41×10^6	$(1.092 \pm 0.002) \times 10^{-12}$	$(9.168 \pm 0.020) \times 10^{-13}$	$(1.014 \pm 0.002) \times 10^{-12}$
1.78×10^6	$(5.947 \pm 0.014) \times 10^{-13}$	$(4.993 \pm 0.013) \times 10^{-13}$	$(5.514 \pm 0.014) \times 10^{-13}$
2.24×10^6	$(3.228 \pm 0.009) \times 10^{-13}$	$(2.705 \pm 0.009) \times 10^{-13}$	$(2.978 \pm 0.009) \times 10^{-13}$
2.82×10^6	$(1.738 \pm 0.006) \times 10^{-13}$	$(1.470 \pm 0.006) \times 10^{-13}$	$(1.610 \pm 0.006) \times 10^{-13}$
3.55×10^6	$(9.301 \pm 0.040) \times 10^{-14}$	$(7.683 \pm 0.036) \times 10^{-14}$	$(8.444 \pm 0.038) \times 10^{-14}$
4.47×10^6	$(4.692 \pm 0.025) \times 10^{-14}$	$(3.902 \pm 0.023) \times 10^{-14}$	$(4.261 \pm 0.024) \times 10^{-14}$
5.62×10^6	$(2.384 \pm 0.016) \times 10^{-14}$	$(1.965 \pm 0.014) \times 10^{-14}$	$(2.133 \pm 0.015) \times 10^{-14}$
7.08×10^6	$(1.159 \pm 0.010) \times 10^{-14}$	$(9.510 \pm 0.090) \times 10^{-15}$	$(1.031 \pm 0.009) \times 10^{-14}$
8.91×10^6	$(5.571 \pm 0.061) \times 10^{-15}$	$(4.529 \pm 0.055) \times 10^{-15}$	$(4.976 \pm 0.058) \times 10^{-15}$
1.12×10^7	$(2.631 \pm 0.037) \times 10^{-15}$	$(2.202 \pm 0.034) \times 10^{-15}$	$(2.321 \pm 0.035) \times 10^{-15}$
1.41×10^7	$(1.265 \pm 0.023) \times 10^{-15}$	$(1.103 \pm 0.022) \times 10^{-15}$	$(1.160 \pm 0.022) \times 10^{-15}$
1.78×10^7	$(6.631 \pm 0.149) \times 10^{-16}$	$(5.818 \pm 0.140) \times 10^{-16}$	$(5.924 \pm 0.141) \times 10^{-16}$
2.24×10^7	$(3.177 \pm 0.092) \times 10^{-16}$	$(2.743 \pm 0.086) \times 10^{-16}$	$(2.787 \pm 0.086) \times 10^{-16}$
2.82×10^7	$(1.651 \pm 0.059) \times 10^{-16}$	$(1.454 \pm 0.056) \times 10^{-16}$	$(1.476 \pm 0.056) \times 10^{-16}$
3.55×10^7	$(8.101 \pm 0.370) \times 10^{-17}$	$(7.048 \pm 0.345) \times 10^{-17}$	$(6.516 \pm 0.331) \times 10^{-17}$
4.47×10^7	$(3.614 \pm 0.220) \times 10^{-17}$	$(3.120 \pm 0.204) \times 10^{-17}$	$(3.038 \pm 0.202) \times 10^{-17}$
5.62×10^7	$(2.146 \pm 0.151) \times 10^{-17}$	$(2.013 \pm 0.146) \times 10^{-17}$	$(1.848 \pm 0.140) \times 10^{-17}$
7.08×10^7	$(9.764 \pm 0.908) \times 10^{-18}$	$(8.343 \pm 0.840) \times 10^{-18}$	$(8.345 \pm 0.840) \times 10^{-18}$
8.91×10^7	$(4.156 \pm 0.528) \times 10^{-18}$	$(4.654 \pm 0.559) \times 10^{-18}$	$(4.086 \pm 0.524) \times 10^{-18}$
1.12×10^8	$(2.694 \pm 0.379) \times 10^{-18}$	$(2.585 \pm 0.371) \times 10^{-18}$	$(2.636 \pm 0.375) \times 10^{-18}$
1.41×10^8	$(1.242 \pm 0.229) \times 10^{-18}$	$(1.286 \pm 0.233) \times 10^{-18}$	$(11.154 \pm 2.174) \times 10^{-19}$
1.78×10^8	$(5.310 \pm 1.337) \times 10^{-19}$	$(5.647 \pm 1.379) \times 10^{-19}$	$(4.922 \pm 1.287) \times 10^{-19}$

knee (Amenomori et al. 2006a, 2006b, 2000) that were derived from the hybrid experiment using the air-shower core detector, which is sensitive to showers of light-element origin such as proton or helium by selecting the high-energy core. From the observed steep power index and the low intensities of proton and helium spectra, the dominance of the heavy elements was suggested by the hybrid experiment; however, the statistics were limited due to the high threshold. In the very near future, we will start a new high-statistics hybrid experiment in Tibet (Huang et al. 2005) to clarify the main component of cosmic rays at the knee. The core detector will consist of 400 burst detectors located at the center of the Tibet-III array in a grid with a detector interval of 3.75 m. The burst detectors measure the high-energy electromagnetic cascade of energy above 30 GeV developed in lead plate 3.5 cm thick by shower core particles. The new experiment is able to observe the air-shower cores induced by heavy components around and beyond the knee, where direct measurements are inaccessible because of their extremely low fluxes. The first observation of the iron spectrum in the knee region is expected in this new experiment.

TABLE 5
SUMMARY OF THE KNEE PARAMETERS

Model	Knee Position (PeV)	Index of Spectrum
QGSJET+Iron	4.4 ± 0.1	$\gamma_1 = -2.81 \pm 0.01$
		$\gamma_2 = -3.21 \pm 0.01$
QGSJET+HD	4.0 ± 0.1	$\gamma_1 = -2.67 \pm 0.01$
		$\gamma_2 = -3.10 \pm 0.01$
QGSJET+PD	3.8 ± 0.1	$\gamma_1 = -2.65 \pm 0.01$
		$\gamma_2 = -3.08 \pm 0.01$
SIBYLL+HD	4.0 ± 0.1	$\gamma_1 = -2.67 \pm 0.01$
		$\gamma_2 = -3.12 \pm 0.01$
QGSJET+Proton	3.4 ± 0.1	$\gamma_1 = -2.60 \pm 0.01$
		$\gamma_2 = -3.03 \pm 0.01$

NOTE.—The symbol γ_1 is the best-fitted index for the energy range 100 TeV $< E_0 <$ 1 PeV, and γ_2 is for the energy above 4 PeV.

The collaborative experiment of the Tibet Air-Shower Arrays has been performed under the auspices of the Ministry of Science and Technology of China and the Ministry of Foreign Affairs of Japan. This work was supported in part by a Grant-in-Aid for Scientific Research on Priority Areas from the Ministry of Education, Culture, Sports, Science, and Technology, by Grants-in-Aid for Science Research from the Japan Society for the Promotion of Science in Japan, and by the Grants-in-Aid from the National Natural Science Foundation of China and the Chinese Academy of Sciences. The authors thank J. Kota for reading the manuscript.

REFERENCES

Aglietta, M., et al. 2004, Astropart. Phys., 20, 641
Amenomori, M., et al. 1990, Nucl. Instrum. Methods Phys. Res. A, 288, 619
———. 1992, Phys. Rev. Lett., 69, 2468
———. 1996, ApJ, 461, 408
———. 2000, Phys. Rev. D, 62, 112002
———. 2003a, in Proc. 28th Int. Cosmic Ray Conf. (Tsukuba), 143
———. 2003b, ApJ, 598, 242
———. 2006a, Phys. Lett. B, 632, 58
———. 2006b, Adv. Space Res., 37, 1938
———. 2007, Adv. Space Res., in press (arXiv:0803.1005)
Antoni, T., et al. 2005, Astropart. Phys., 24, 1
Apanasenko, A. V., et al. 2001, Astropart. Phys., 16, 13
Asakimori, K., et al. 1998, ApJ, 502, 278
Berezhko, E. G., & Ksenofontov, L. G. 1999, J. Exp. Theor. Phys., 89, 391
Bloomer, S. D., Linsley, J., & Watson, A. A. 1988, J. Phys. G, 14, 645
Bonechi, L., et al. 2006, in AIP Conf. Proc. 867, The LHCf Experiment at the LHC Accelerator (New York: AIP), 266
Candia, J., Roulet, E., Epele, L. N. 2002, J. High Energy Phys., 12, 33
Erlykin, A. D., & Wolfendale, A. W. 2005, Astropart. Phys., 23, 1
Fowler, J. W., et al. 2001, Astropart. Phys., 15, 49
Glasmacher, M. A. K., et al. 1999, Astropart. Phys., 10, 291
Grigorov, N. L., et al. 1971, in Proc. 12th Int. Cosmic Ray Conf. (Hobart), 1746
Heck, D., Knapp, J., Capdevielle, J. N., Schatz, G., & Thouw, T. 1998, CORSIKA: A Monte Carlo Code to Simulate Extensive Air Showers (FZKA Rep. 6019; Karlsruhe: Forschungszentrum Karlsruhe)
Hörandel, J. R. 2003, Astropart. Phys., 19, 193
———. 2004, Astropart. Phys., 21, 241
Huang, J., et al. 2005, in Proc. 29th Int. Cosmic Ray Conf. (Pune), 173
Kobayakawa, K., et al. 2002, Phys. Rev. D, 66, 083004
Nagano, M., Hara, T., Hatano, Y., Hayashida, N., Kawaguchi, S., Kamata, K., Kifune, T., & Mizumoto, Y. 1984, J. Phys. G, 10, 1295
Nagano, M., et al. 1992, J. Phys. G, 18, 423
Nikolsky, S. I., & Romachin, V. A. 2000, Phys. At. Nuclei, 63, 1799
Ogio, S. 2004, ApJ, 612, 268
Ptuskin, V. S., et al. 1993, A&A, 268, 726
Roth, M., et al. 2007, in Proc. 30th Int. Cosmic Ray Conf. (Merida), in press (arXiv:0706.2096)
Sako, T., et al. 2007, Nucl. Instrum. Methods Phys. Res. A, 578, 146
Stanev, T., et al. 1993, A&A, 274, 902
Takeda, M., et al. 2003, Astropart. Phys., 19, 447
Völk, H. J., & Zirakashvili, V. N. 2004, A&A, 417, 807
Wigmans, R. 2003, Astropart. Phys., 19, 379
Yamamoto, T., et al. 2007, in Proc. 30th Int. Cosmic Ray Conf. (Merida), in press (arXiv:0707.2638)